Research Article | Vol. 30, No. 20 / 26 Sep 2022 / Optics Express 35282
Optics EXPRESS

Elastic net-based non-negative iterative three-operator splitting strategy for Cerenkov luminescence tomography

YI CHEN,[1] WEITONG LI,[1,2] MENGFEI DU,[1,2] LINZHI SU,[1,2,4] HUANGJIAN YI,[1] FENGJUN ZHAO,[1] KANG LI,[1,2] LIN WANG,[3] AND XIN CAO[1,2,5]

[1]School of Information Science and Technology, Northwest University, Xi'an, Shaanxi 710127, China
[2]National and Local Joint Engineering Research Center for Cultural Heritage Digitization, Xi'an, Shaanxi 710127, China
[3]School of Computer Science and Engineering, Xi'an University of Technology, Xi'an, Shaanxi 710048, China
[4]sulinzhi029@163.com
[5]xin_cao@163.com

Abstract: Cerenkov luminescence tomography (CLT) provides a powerful optical molecular imaging technique for non-invasive detection and visualization of radiopharmaceuticals in living objects. However, the severe photon scattering effect causes ill-posedness of the inverse problem, and the location accuracy and shape recovery of CLT reconstruction results are unsatisfactory for clinical application. Here, to improve the reconstruction spatial location accuracy and shape recovery ability, a non-negative iterative three operator splitting (NNITOS) strategy based on elastic net (EN) regularization was proposed. NNITOS formalizes the CLT reconstruction as a non-convex optimization problem and splits it into three operators, the least square, $L_{1/2}$-norm regularization, and adaptive grouping manifold learning, then iteratively solved them. After stepwise iterations, the result of NNITOS converged progressively. Meanwhile, to speed up the convergence and ensure the sparsity of the solution, shrinking the region of interest was utilized in this strategy. To verify the effectiveness of the method, numerical simulations and *in vivo* experiments were performed. The result of these experiments demonstrated that, compared to several methods, NNITOS can achieve superior performance in terms of location accuracy, shape recovery capability, and robustness. We hope this work can accelerate the clinical application of CLT in the future.

© 2022 Optica Publishing Group under the terms of the Optica Open Access Publishing Agreement

1. Introduction

Cerenkov radiation (CR) was discovered back in 1934, it occurs when a charged particle propagates faster than the speed of light in the propagation medium [1]. In 2009, Roberson et al. first used the radionuclides of 2-18fluoro-D-glucose (^{18}F-FDG) for optical molecular imaging. This optical molecular imaging method was termed Cerenkov luminescence imaging (CLI) [2,3]. Because CLI combines the advantages of the higher throughput and the low-cost imaging, CLI has attracted widespread attention [4,5]. At present, CLI has been used in preclinical and clinical studies, such as tumor localization, drug evaluation, endoscopy, surgery guidance, and other fields [6–10]. However, CLI can only provide 2D information of the surface radioactive probe and lacks depth information, so it cannot infer the location of the internal source [11]. Therefore, Cerenkov luminescence tomography (CLT) was proposed, which can obtain the 3D spatial distribution of interior radioactive probes [12–14].

Like other optical tomography reconstruction technologies, CLT has the problem of ill-posed due to the serious scattering of Cerenkov photons in the tissue [15], resulting in insufficient

#465501 https://doi.org/10.1364/OE.465501
Journal © 2022 Received 1 Jun 2022; revised 1 Aug 2022; accepted 18 Aug 2022; published 13 Sep 2022

Optics EXPRESS

spatial positioning accuracy and shape recovery [16], which is a great challenge to the clinical application of CLT. To improve the performance of CLT reconstruction, some anatomical prior information and regularization methods can be added to CLT reconstruction. In the first CLT reconstruction experiment of small animals, it is assumed that the optical properties of mouse tissues are consistent and uniform [12], but this assumption is not consistent with the real situation. Later, Hu et al. proposed a heterogeneous mouse model. By using mouse anatomical information and different optical properties of organs, this model can reduce the systematic error of CLT and significantly improve the accuracy of tumor localization [17]. Moreover, some regularization theories are gradually applied to CLT reconstruction to ensure the accuracy of Cerenkov source, such as L_2-norm regularization (Tikhonov method) [12], L_1-norm regularization (Lasso method) [18,19] and L_p-norm ($0 < p < 1$) regularization (non-convex method) [20]. However, these regularization methods have their defects. L_2-norm regularization will introduce many artifacts of reconstruction, resulting in excessive smoothing of the results [21]. L_1-norm regularization and L_p-norm regularization cause other problems in the reconstruction results, such as over-sparseness and lack of fluorescence probe boundary information [22]. To overcome these shortcomings, Some methods based on joint regularization were proposed, such as difference of convex algorithm (DCA) based on L_{1-2}-norm [23], Sparse-graph manifold learning (SGML) method [24] and so on [25–27]. In addition, many researchers found that shrinking the region of interest (ROI) can also improve the reconstruction accuracy of optical tomography reconstruction [28,29]. These works provide some new ideas for alleviating the ill-posedness of CLT reconstruction. In addition to traditional mathematical methods, deep learning strategies are also introduced in CLT [30–32]. In 2019, a CLT approach based on multi-layer fully connected networks was proposed [33]. Subsequently, the attention mechanism of deep learning and decoder-encoder and other structures are also used to reconstruct the Cerenkov source [30,32,34]. Although the neural network method improves the performance of CLT reconstruction, it not only needs a huge amount of training data but also has weak generalization ability, that is, the trained artificial neural network can only be applied to specific imaging objects [35].

In this work, a non-negative iterative three-operator splitting (NNITOS) approach based on elastic net (EN) was proposed to improve the accuracy and robustness of CLT reconstruction. EN regularization combined the advantages of $L_{1/2}$-norm regularization and manifold learning regularization. The inverse problem of CLT source reconstruction was transformed by NNITOS into a nonconvex, nonnegative iterative, and mixed regularization minimization problem. Based on EN regularization, the objective minimum optimization function of the inverse problem was split into the least square operator, the $L_{1/2}$-norm regularization operator, and the manifold learning regularization operator using NNITOS. The optimal solution of this objective optimization function was approximated by solving the indeterminate point equation, and because the Cerenkov source was non-negativity, a non-negative constraint was added to the solution of this method. To further speed up the convergence of the solution of the indeterminate point equation, we used a shrinking ROI strategy to constrain the region of the next step solution based on the results of the previous step during the iterative process of the solution.

To evaluate the performance of NNITOS based on EN regularization in CLT reconstruction, numerical simulation and *in vivo* experiments were carried out. Compared with fast iterative shrinkage thresholding algorithm (FISTA) based on L_1-norm [36], incomplete variables truncated conjugate gradient (IVTCG) algorithm based on L_1-norm [37], Gaussian weighted Laplace prior (GWLP) based on L_2-norm [38]. The experimental results show that the reconstruction accuracy and shape recovery ability are greatly improved by NNITOS.

The structure of the rest of this paper is as follows. Section 2 introduces the CLT forward model, CLT inverse problem and NNITOS strategy. Section 3 introduces the process and results of numerical simulation and *in vivo* experiments. Section 4 makes some discussion and summary of this paper.

Optics EXPRESS

2. Methodology

2.1. Forward model of CLT

The transmission of Cerenkov photons in biological tissue accords with the Radiative Transfer Equation (RTE), but it has high computational complexity. In the process of biological tissue transmission, the scattering rate of photons is greater than the absorption rate [39], so RTE can be simplified as a Diffusion Approximation (DA) model. The DA model combined with the Robin boundary condition can be expressed as [40,41]:

$$\begin{cases} -\nabla \cdot (D(r) \cdot \nabla \Phi(r)) + \mu_\alpha(r)\Phi(r) = S(r), (r \in \Omega) \\ \Phi(r) + 2A(r, n, n')D(r)(v(r) \cdot D(r)) = 0, (r \in \partial\Omega) \end{cases} \tag{1}$$

where r represents the nodes in the solution domain Ω. $\partial\Omega$ is boundary of the domain. $\Phi(r)$ denotes the photon flow rate at the node r. $S(r)$ represents Cerenkov source distribution. $D(r) = 1/3(\mu_\alpha(r) + (1-g)\mu_s(r))$, where $\mu_\alpha(r)$ and $\mu_s(r)$ are optical absorption coefficient and optical scattering coefficient of photons at node r, respectively, and g is the medium anisotropy factor. $A(r, n, n') \approx \frac{1+R(r)}{1-R(r)}$, where R(r) is the inner reflection coefficient, n and n' are the refractive index within Ω and the refractive index of external medium, respectively. $v(r)$ denotes the unit outer normal on $\partial\Omega$. Based on the finite element framework [41], the light propagation model can be discretized, and the relationship between the unknown Cerenkov source distribution and the luminous flux on the surface of biological tissue can be described as the linear equation as:

$$Y = UX \tag{2}$$

where Y is the luminous flux measured on the surface, U denotes the system weight matrix and X represents the unknown internal Cerenkov source distribution. Therefore, the purpose of the CLT inverse problem is to restore the radioactive probe distribution X in the above linear equation, and the detailed information of the forward model can be found in [42].

2.2. Inverse problem

As mentioned above, the linear relationship between the Cerenkov luminescence source and the surface luminous flux in biological tissues has been established. As the result of the non-negativity of the Cerenkov source distribution, and inspired by Three-Operator Splitting (TOS) algorithm [43,44], the NNITOS approach for CLT was proposed to alleviate the ill-posedness of the inverse problem. The TOS algorithm is described by the most straightforward mathematical formula as:

$$\Phi(X) = \ minimize\ f(X) + g(X) + h(X) \tag{3}$$

where Φ is expressed as our objective function, f is potentially nonconvex and Lipschitz differentiable, and g and h are convex functions and potentially non-smooth. Combining the TOS algorithm and the objective function of CLT reconstruction, our proposed objective function can be expressed as follows:

$$\min_X \frac{1}{2} \|UX - Y\|_2^2 + \lambda_1 \|X\|_{\frac{1}{2}}^{\frac{1}{2}} + \lambda_2 X^T L X \tag{4}$$

where λ_1 and λ_2 are the regularization parameters, $\|X\|_{\frac{1}{2}}^{\frac{1}{2}} = \Sigma_i \sqrt{|x|}$ denotes a quasi-norm, $X^T L X$ is the Laplacian manifold regularization term and L is the dynamic graph Laplacian matrix. This combination of different norms is called EN regularization [45,46]. The details of the EN-based NNITOS method are described below.

Optics EXPRESS

2.2.1. EN regularization

The EN regularization proposed by us included $L_{1/2}$-norm regularization and manifold regularization. The EN combines two different regularizations, which can combine the advantages of each regularization, so it finds a balance between the sparsity and stationarity of the results. L_p-norm regularization can produce more sparse solutions than L_1-norm regularization, and $L_{1/2}$-norm regularization is representative among all L_p-norm regularizations with p in (0, 1) [47]. Thus, we choose $L_{1/2}$-norm regularization instead of L_1-norm regularization. As a popular learning method, manifold learning is often used to constrain local linear relations [48,49]. We can use manifold learning techniques to explore the geometric characteristics of data distribution [50]. To improve the accuracy of the solution space, in the manifold regularization term, we propose an adaptive grouping that adjusts the grouping according to the intensity of the grid nodes, as shown in Fig. 1. In the finite element framework, the strength of each mesh node is closely related to the tetrahedron, and the central node $\tilde{x}_i$ is shared by multiple tetrahedrons in Fig. 1. Therefore, the strength of the i-th node is transformed into the strength of the i-th group, the n_i represents the initial length of the i-th group, and the threshold is $E_i = X_i/n_i$, where X_i is the sum of the energy values of the i-th group. Nodes whose intensity is less than the threshold will be removed from the group. The initial length of each group may be different, but in this paper, $n_i = 9$, refer to related work [51]. In the adaptive grouping, we construct the adjacency matrix g. If the i-th node and the j-th node were in the same group, then $g_{ij} = 1$, otherwise, $g_{ij} = 0$.

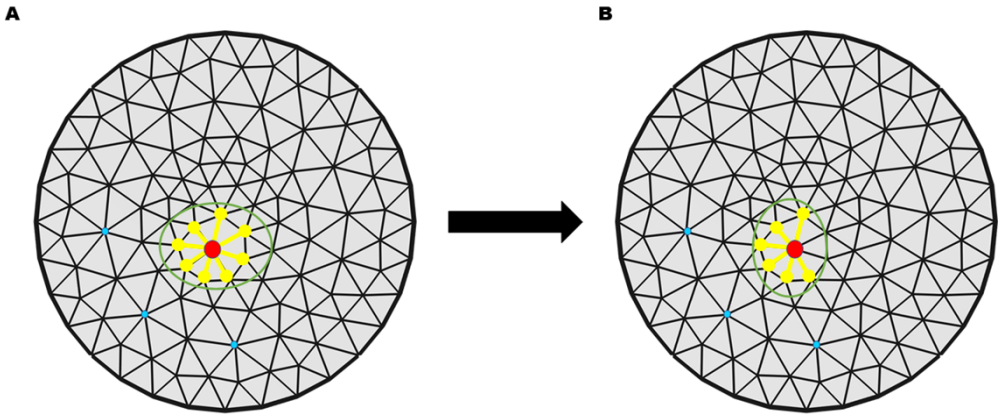

Fig. 1. The schematic diagram of adaptive grouping. (A) represents the initial group, with the red node as the center node $\tilde{x}_i$, the yellow node surrounded by the green oval region is the neighbors of $\tilde{x}_i$, the $g_{ij} = 0$ of the blue node. (B) indicates that after the adjustment of the group, the nodes whose energy value is less than the threshold E_i are excluded from the green ellipse region.

The adjacency matrix g is needed in solving the dynamic graph Laplacian matrix L in EN regularization. The Laplacian manifold regularization term is defined as:

$$\sum_{i=1}^{N}\sum_{j=1}^{N} w_{ij}(x_i - x_j)^2 \tag{5}$$

where x_i and x_j denote i-th node and the j-th node, N is the number of finite elements meshes, and w_{ij} is the weight of the edge between node N_i and node N_j. The w_{ij} is defined as:

$$w_{ij} = \begin{cases} exp(-\frac{\|N_i - N_j\|_2^2}{4R^2}) \\ 0\ ,\ i = j\ or\ g_{ij} = 0 \end{cases} \Big/ \sum exp\left(-\frac{N_i - N_{j2}^2}{4R^2}\right) \quad ,\ g_{ij} = 1 \tag{6}$$

Optics EXPRESS

where $\left\|N_i - N_j\right\|_2^2$ is the Euclidean distance between the i-th node and the j-th node, R is the radius of the Gaussian kernel function which adjusts the probability density function of adjacent nodes, $g_{ij} = 1$ means that the i-th node and the j-th node are in the same group, whereas $g_{ij} = 0$ means that the i-th node and the j-th node are not in the same group, as shown in Fig. 1. Obviously, $w_{ij} \in [0, 1]$. After a simple mathematical derivation, Eq. (4) can be simplified to $2X^T(D - W)X$, where W is an asymmetrical weight matrix, which equivalents to $(w_{ij})_{NN}$. D is the entry diagonal matrix of the vertex, which is defined as:

$$D_{ij} = \begin{cases} \sum_{j=1}^{N} W_{ij}, & i = j \\ 0, & i \neq j \end{cases} \tag{7}$$

Let $L = D - W$, we will get the dynamic graph Laplacian matrix proposed by Eq. (4).

2.2.2. NNITOS strategy based on EN

In this section, NNITOS will be explained in detail. When we combine Eq. (3) and Eq. (4), it can be expressed as follows:

$$\begin{cases} f(X) = \lambda_1 \|X\|_{\frac{1}{2}}^{\frac{1}{2}} \\ g(X) = \frac{1}{2}\|UX - Y\|_2^2 \\ h(X) = \lambda_2 X^T L X \end{cases} \tag{8}$$

where λ_1 and λ_2 are selected empirically, which are given in related works [52,53]. It is noted that NNITOS solved our objective function by evaluating the terms h and $(f + g)$ at two different points, x and z. $(f(x) + g(x)) + h(z)$ can be equal to the optimal object value, even if x and z are not close to the solution. We can introduce the distance condition between x and z to address this issue. The following definition of an α-close and β-stationary pair of points is crucial for solving the Eq. (3):

$$\|\bar{z} - \bar{x}\| \leq \alpha \tag{9}$$

$$\nabla f(\bar{x}), \bar{z} - z + g(\bar{x}) - g(z) + h(\bar{x}) - h(x) \leq \beta \tag{10}$$

where $\langle \cdot, \cdot \rangle$ denote the standard Euclidean inner product associated with the norm $\|\cdot\|$. α-close β-stationary points $(\bar{x}, \bar{z})$ yield approximate solution to Eq. (3) under appropriate assumptions. For specific assumptions, please refer to the Ref. [54]. By Eq. (9) and Eq. (10) we can know that TOS algorithm is approximately stationary. The TOS algorithm is represented by a fixed-point equation as follows:

$$\begin{cases} x_k = prox_{\gamma_k g}(y_k) \\ z_k = prox_{\gamma_k h}(2x_k - y_k - \gamma_k \nabla f(x_k)) \\ y_{k+1} = y_k - x_k + z_k \end{cases} \tag{11}$$

where the proximal operator of function $\dot{g}$ is defined by $prox_{\gamma_k \dot{g}}(y_k) := \underset{y}{argmin}\left\{\dot{g}(y) + \frac{1}{2\gamma_k}\|y - y_k\|^2\right\}$, x_k is the intermediate solution in the iterative process, γ_k is the step-size, k denotes the number of

Optics EXPRESS

iterative rounds. Therefore, Eq. (11) is denoted as:

$$\begin{cases} x_k \in \underset{x}{argmin} \left\{ g(x) + \frac{1}{2\gamma} \|x - y_k\|_2^2 \right\} \\ z_k \in \underset{z}{argmin} \left\{ h(z) + \frac{1}{2\gamma} \|z - (2x_k - y_k - \gamma \nabla f(x_k)\|_2^2 \right\} \\ y_{k+1} = y_k - x_k + z_k \end{cases} \tag{12}$$

By designing a well-behaved fixed-point equation, the TOS method decomposes the minimization of the objective function into solving the nearest neighbor mapping of two individuals. When we combine Eq. (8) and Eq. (12), by solving the partial differential, it can be expressed as follows:

$$\begin{cases} x_k = \left(U^T U + \frac{1}{\gamma_k} I \right)^{-1} \left(U^T Y + \frac{1}{\gamma_k} y_k \right) \\ z_k = \left(\lambda_1 (L^T + L) + \frac{1}{\gamma_k} I \right)^{-1} \left(2x_k - \gamma_k \lambda_2 \left(\frac{1}{2\sqrt{x_k}} \right) - y_k \right) \\ y_{k+1} = y_k - x_k + z_k \end{cases} \tag{13}$$

where the I denotes the unit matrix of $N \times N$. The value of γ_1 is selected refer to related work [44]. We add non-negative constraints to the TOS algorithm. In addition, NNITOS method uses ROI framework. In each iteration, we shrink the ROI based on the results of the iteration. Therefore, the NNITOS method for solving the inverse CLT problem can be summarized as Algorithm 1.

Algorithm 1 NNITOS

Input: The system matrix U and the measured luminous flux vector Y.

Initialization: The global R_0 as the initial ROI, set vector $y_1 = 0$, set step-size $\gamma_1 = 0.15$, iteration index $k = 1$, the regularization parameters $\lambda_1 = \lambda_2 = 1e-5$, the cosine similarity $EC_k = 0$, Euclidean distance $EL_k = 0$.

Step1: Find the nine nearest neighbors of each node and assign them to the same group, construct the adjacency matrix g. calculate the threshold E_i for each group.$g_{ij} = 0$ denote the j-th node is not in the i-th group.

Step2: Calculate the dynamic graph Laplacian matrix L, via the Eq. (5), (6) and (7).

Repeat

Step3: Utilize the Eq. (13) to update x_k, z_k, y_{k+1}, The point less than 0 in x_k is set to 0.

Step4: Calculate the cosine similarity EC_{k+1} and Euclidean distance EL_{k+1} between Ux_k and Y.

Step5: Shrinking the ROI according to the reconstruction result x_k, set the node with lower energy value in x_k to 0.

Step6: Increase the iteration index $k = k + 1$, and then update step-size $\gamma_k = max\left\{\frac{\gamma_{k-1}}{2}, 0.9999 \times \gamma_{k-1}\right\}$.

Until $EC_k \langle EC_{k-1}$ *or* $EL_k \rangle EL_{k-1}$.

Output: x_k.

3. Experiments and results

To verify and systematically evaluate the performance of NNITOS in CLT reconstruction, four groups of simulation experiments and one group of *in vivo* experiments were introduced in this

Optics EXPRESS

paper. Three types of algorithms were compared with our proposed methods, namely, FISTA algorithm based on L_1-norm, IVTCG algorithm based on L_1-norm, and GWLP based on L_2-norm. The regularization parameters of these algorithms come from related work [26,18]. In addition, to assess the stability, we also carried out a group of anti-Gaussian noise experiments with dual-source. All the programs in this work were executed on desktop computers with an Intel Core i3-10100 CPU (3.60 GHz) and 8GB RAM.

3.1. Evaluation metrics

To evaluate the location accuracy, shape recovery ability, and source intensity accuracy of CLT reconstruction in ROI, the location error (LE), DICE similarity coefficient (DICE), relative intensity error (RIE), and contrast to noise ratio (CNR) were taken as the quantitative evaluation indexes. LE represents the error between the center position of the reconstruction source and the center position of the real source, which is defined as:

$$LE = \|L(X_r) - L(X_t)\| \tag{14}$$

where X_r denotes the vector of the reconstructed source and X_t denotes the vector of the true source. DICE is the similarity between the reconstructed source region and the real source region:

$$DICE = 2\frac{|R_r \cap R_t|}{|R_r| + |R_t|} \tag{15}$$

where R_r denotes the region of the reconstructed source and R_t denotes the region of the true Cerenkov source. DICE values range from 0 to 1, and the closer the DICE is to 1, the higher the shape recovery of the reconstruction source. RIE is used to evaluate the relative intensity error between the reconstructed Cerenkov source intensity and the actual Cerenkov source intensity:

$$RIE = \frac{|I_r - I_t|}{I_t} \tag{16}$$

where I_r denotes the intensity of the reconstructed source and I_t denotes the intensity of the true Cerenkov source. Obviously, the closer the RIE is to 0, the better the intensity recovery of the reconstructed source. The contrast to noise ratio (CNR) is used to evaluate the quality of reconstruction results, and CNR is defined as follows:

$$CNR = \frac{|\mu_{ROI} - \mu_{BCK}|}{\left(m_{ROI}\sigma^2_{ROI} + m_{BCK}\sigma^2_{BCK}\right)^{1/2}} \tag{17}$$

where μ_{ROI} and μ_{BCK} represent the mean values in the ROI and background, respectively; σ^2_{ROI} and σ^2_{BCK} are represent the variances; and m_{ROI} and m_{BCK} represent the number of nodes included in the ROI and background, respectively. The higher value of CNR indicates better quality of the reconstruction.

3.2. Experimental process

3.2.1. Numerical simulation

A series of numerical simulations are carried out based on the cylinder model, the main components of the cylinder model are shown in Fig. 2(A). It consists of five organs: muscle, heart, lung, liver, and bone. Moreover, all experiments in this work are based on single spectrum (650 nm). Here, the optical parameters of these organs at 650 nm are consistent with those in Ref. [35,55], as shown in Table 1. In all simulations, for the inverse reconstruction, the cylinder model was discretized into a uniform tetrahedral mesh, including 4626 nodes and 25840 tetrahedral elements using Comsol Multiphysics software [56], and the mean element edge size is 1.37mm,

Optics EXPRESS

as shown in Fig. 2(B). the molecular optical simulation environment (MOSE) platform [57] based on the Monte Carlo method was used to simulate the surface flux distribution, as shown in Fig. 2(C).

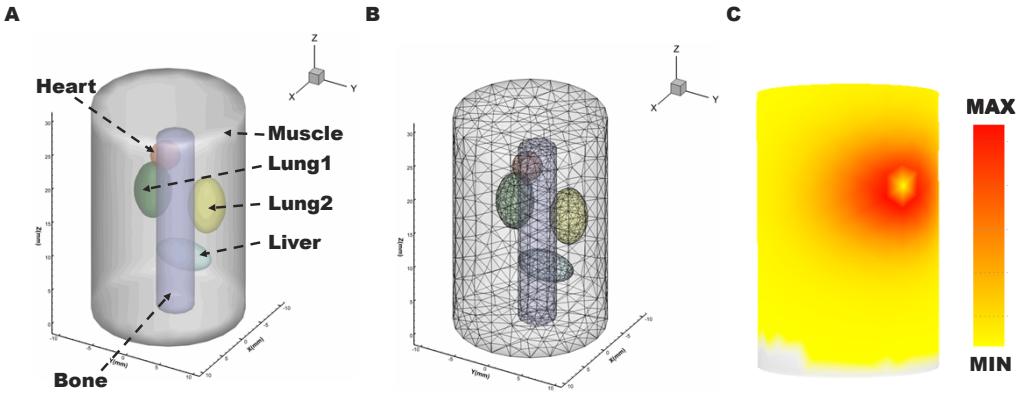

Fig. 2. (A) The numerical phantom-based physical model. (B) Application of tetrahedral mesh of physical model in CLT inverse problem. (C) shows the forward simulation result.

Table 1. Optical coefficients used in numerical simulation

Tissues	$\mu_\alpha(mm^{-1})$	$\mu_s(mm^{-1})$	g
Muscle	0.016	0.510	0.90
Heart	0.011	1.053	0.86
Bone	0.021	2.864	0.90
Liver	0.065	0.723	0.90
Lung	0.036	2.246	0.90

We simulated Cerenkov sources of different sizes, shapes, and positions in organisms. The specific shapes, sizes, and positions of these light sources were shown in Table 2. Four groups of simulation experiments were designed. In one group of experiments, a spherical single light source with a radius of 1mm and 1.5mm was placed at the central coordinate (3, 3, 5) mm, while in the other group, a spherical single light source and a cube single light source with the same radius were placed at the central coordinate (0, -1, 25) mm. These experiments evaluate the shape recovery accuracy of NNITOS by simulating a single source with different positions and different shapes. We also carried out a dual-source simulation experiment to assess the spatial positioning accuracy. The central coordinates of the dual-source were (3, 3, 8) mm and (3, 3, 16) mm, respectively. Finally, to assess the robustness of NNITOS, we designed a set of anti-noise simulation experiment. Specifically, 5%, 10%, 15%, 20%, 25% Gaussian noise was added to the 1.0 mm spherical dual-source simulation experiment with central coordinates of (0, -2, 15) mm and (0, -2, 25) mm.

3.2.2. Implanted animal experiments

To further access the performance of our proposed method, we used the experimental data of implanted adult nude mouse (about 6-8 weeks old/female) and used a CLT/micro-CT dual-modality imaging system to acquire experimental data. Implanted animal experiments were carried out under 2% isoflurane-oxygen mixture gas anesthesia to minimize the suffering of the mouse. All procedures were conducted under the protocols approved by the Animal Ethics Committee of the Northwest University of China and Use Committee.

Optics EXPRESS

Table 2. Cerenkov source settings in numerical simulation

Simulation	Source Shape	Source Size (mm)	Center(mm)	Intensity
Single-source	Spherical	1mm	(3, 3, 5)	1
	Spherical	1.5mm	(3, 3, 5)	1
	Cube	1mm	(0, -1, 25)	1
	Spherical	1mm	(0, -1, 25)	1
Dual-source	Spherical	1mm	S1: (3, 3, 8)	1
		1mm	S2: (3, 3,16)	1
	Spherical	1mm	S1: (0,- 2, 15)	1
		1mm	S2: (0, -2, 25)	1

In the experiment, firstly, we used a spherical glass vessel with a radius of 1 mm containing about $800 \pm 50\mu$Ci ^{18}F-FDG as the artificial Cerenkov luminescence source, and then implanted it into mouse at the designed locations. Secondly, we began to collect the dual-modality raw data. The mouse was placed on the automatic rotating stage, which was rotating 360 degrees with 1° intervals to capture the images of CLI and X-ray projection. By using band-pass filters (FF01-650/13-25, Semrock, USA). The CLI signal with wavelength of 650nm and white light data were collected by a cooled high-sensitivity EMCCD (-80°C, iXonEM Ultra 888, UK). Before acquisition process of CLT, it is set that long exposure time (5min), high given value (300), high shift speed (13μs), and low speed readout rate (1MHz at 16bits). Then CT volume data was acquired by a micro-CT system (tube voltage of 40kV p, tube current of 300mA).

After *in vivo* imaging, we proceeded with data processing, as shown in Fig. 3(C), the trunk sections of the mouse with a height of 41mm was obtained. We segmented the main organs of the mouse, including muscle, lung, heart, stomach, liver, and kidney, and integrated these organs into the mouse model. The optical parameters of each organ are consistent with those in the literature [58]. It should be noted that, the mouse was used for three times, and each time the location of the implanted radionuclide probe is different ((17.5, 23.0, 21.0) mm, (14.5, 26.0, 33.0) mm, and (14.5, 20.0, 36.0) mm)). Moreover, the CLI images obtained from each implanted model was mapped and registered to the surface of the mouse torso. To assess the feasibility of this method *in vivo*, NNITOS was also compared with the other three algorithms mentioned above.

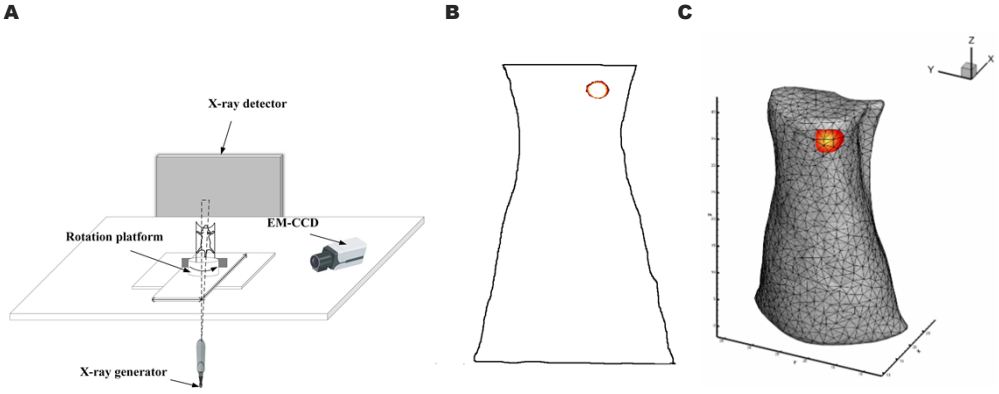

Fig. 3. (A) The schematic diagram of device structure of CLT/micro-CT dual-mode system. (B) shows the plane CLI photon distribution in a certain position of the mouse. (C) shows the distribution of Cerenkov source at a certain location in mouse.

Optics EXPRESS

3.3. Results

3.3.1. Multi-sized and multi-shape single-source reconstruction

In terms of shape restoration ability, we compare the performance of NNITOS and the above three algorithms in a single source of different sizes and different shapes. The results of 3D reconstruction and the shape of the axial plane prove the effectiveness of our proposed method. As shown in Fig. 4 and Fig. 5, the reconstructed Cerenkov source was represented by a red region under 3D-view. Figure 4 showed the comparative results of using different methods to reconstruct a single source of different sizes, and Fig. 5 showed the comparative results of using different methods to reconstruct a single source of different shapes. These two experiments showed that the reconstruction result of the NNITOS method is closer to the real source. According to Table 3 and Table 4, we found that the NNITOS had a smaller LE, so the reconstructed Cerenkov source center is closer to the real value, and the DICE of NNITOS is smaller, indicating that the reconstructed Cerenkov source region and the actual Cerenkov source region have a good overlap, and the RIE of NNITOS is lower, means that the energy intensity recovery rate of the reconstructed source is very high.

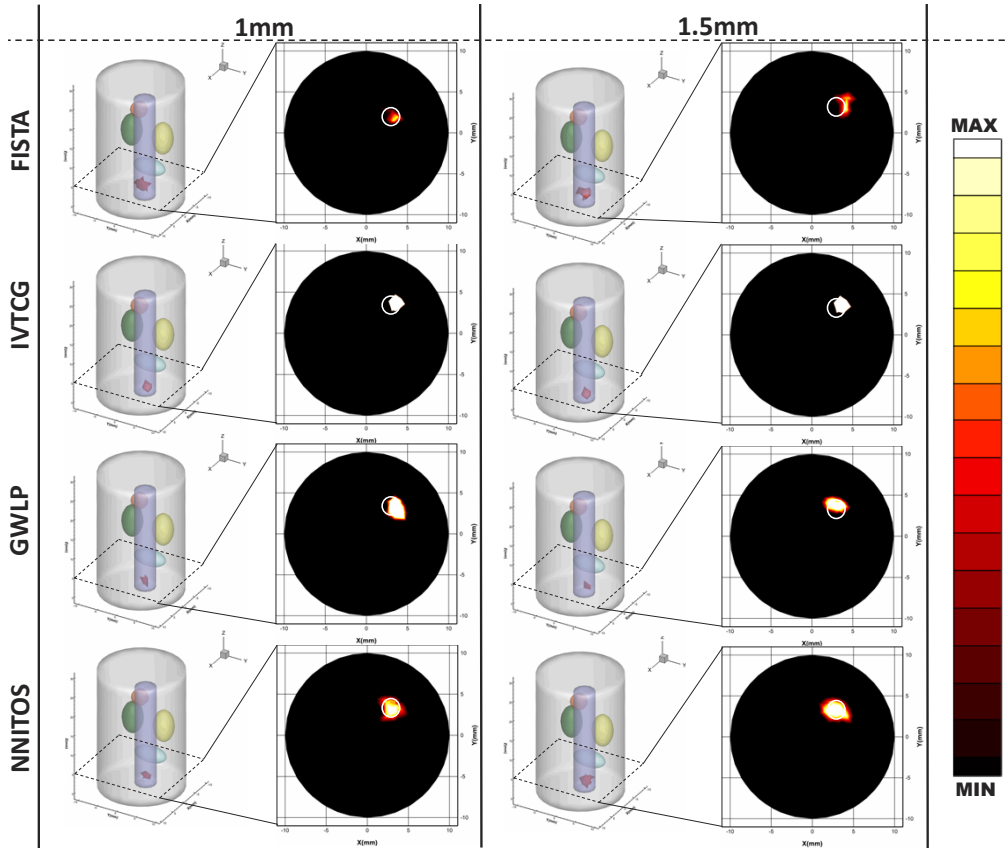

Fig. 4. Reconstruction results of simulation experiments of single spherical source of different sizes. The reconstruction result is cut along the z-axis of the Cerenkov source to obtain the axial view, and the white circle on the plan represents the real location and size of the source.

Optics EXPRESS

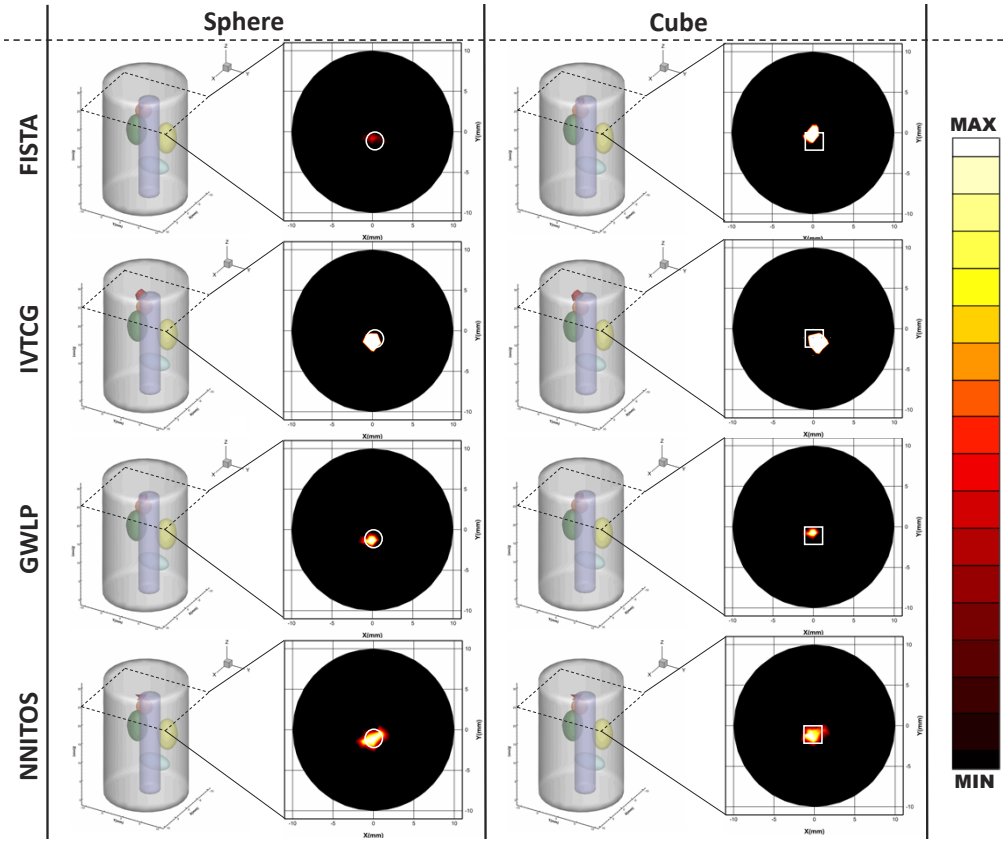

Fig. 5. The reconstruction results of single source simulation experiments with different shapes. The reconstruction result is cut along the z-axis of the Cerenkov source to obtain the axial view. The white circle on the plane represents the real location and size of the sphere source, and the white square is the real location and size of the cube source.

Table 3. Quantitative analysis of multi-sized single-source simulation reconstruction results

Size	Actual source center (mm)	Method	LE (mm)	DICE	RIE	CNR
1	(3, 3, 5)	FISTA	0.967	0.562	1.567	0.292
		IVTCG	0.837	0.374	1.985	0.405
		GWLP	0.606	0.754	1.173	0.983
		NNITOS	0.126	0.911	0.192	1.369
1.5	(3, 3, 5)	FISTA	1.374	0.324	0.669	0.186
		IVTCG	0.981	0.386	0.962	0.223
		GWLP	0.892	0.388	0.709	0.76
		NNITOS	0.32	0.704	0.058	0.853

Optics EXPRESS

Table 4. Quantitative analysis of multi-shape single-source simulation reconstruction results

Shape	Actual source center (mm)	Method	LE (mm)	DICE	RIE	CNR
Sphere	(0, -1, 25)	FISTA	0.996	0.496	0.745	0.287
		IVTCG	0.641	0.51	1.773	0.361
		GWLP	0.428	0.48	0.694	0.866
		NNITOS	0.199	0.933	0.206	1.337
Cube	(0, -1, 25)	FISTA	0.704	0.429	0.976	0.252
		IVTCG	0.692	0.444	1.927	0.333
		GWLP	0.576	0.472	0.721	0.799
		NNITOS	0.357	0.84	0.272	1.253

3.3.2. Dual-source reconstruction

To further verify the positioning accuracy of NNITOS reconstruction, we have established a dual-source experiment. Different methods of reconstruction of Cerenkov dual spherical sources are shown in 3D, axial, sagittal and coronal views as shown in Fig. 6. FISTA and IVTCG produce excessive smoothing artifacts around a single source. Although the reconstruction performance of GWLP is better than that of the former two methods, compared with NNITOS, the center position of NNITOS reconstruction is more accurate, the image artifacts are less, and the light source intensity is closer to the real value. Specifically, the quantitative analysis of the reconstruction results of dual-source simulation is shown in Table 5.

Table 5. Quantitative analysis of dual-source simulation reconstruction results

Method	Actual source center (mm)	LE (mm)	Total LE (mm)	DICE	RIE	CNR
FISTA	(3, 3, 8)	1.123	2.179	0.433	1.518	0.109
	(3, 3, 16)	1.056		0.525	1.596	
IVTCG	(3, 3, 8)	1.089	2.217	0.48	1.693	0.133
	(3, 3, 16)	1.128		0.393	0.743	
GWLP	(3, 3, 8)	0.898	1.933	0.497	0.773	0.284
	(3, 3, 16)	1.035		0.47	0.715	
NNITOS	(3, 3, 8)	0.314	0.565	0.871	0.405	0.41
	(3, 3, 16)	0.251		0.899	0.237	

3.3.3. Anti-noise performance

To test the robustness of NNITOS, we established an anti-noise experiment. The dual-source simulation as an example, 5% 10% 15% 20% 25% Gaussian noise was added to detect the impact on NNITOS reconstruction results. As shown in Fig. 7, the values of LE, DICE, RIE and CNR fluctuate little, indicating that the method is robust to noise.

3.3.4. Implanted animal experiment

To evaluate the practicability of NNITOS imaging *in vivo*, we used the experimental data of a mouse with radioactive probes *in vivo*. According to the mouse trunk boundary registration, the reconstruction results obtained by different methods are shown in Fig. 8. The three-dimensional reconstruction results and axial plane prove the effectiveness of different methods, our proposed method successfully overcame the over-smooth problem *in vivo* experiment. NNITOS has the smallest LE, the largest source matching area, and the best energy recovery ability, and

Optics EXPRESS

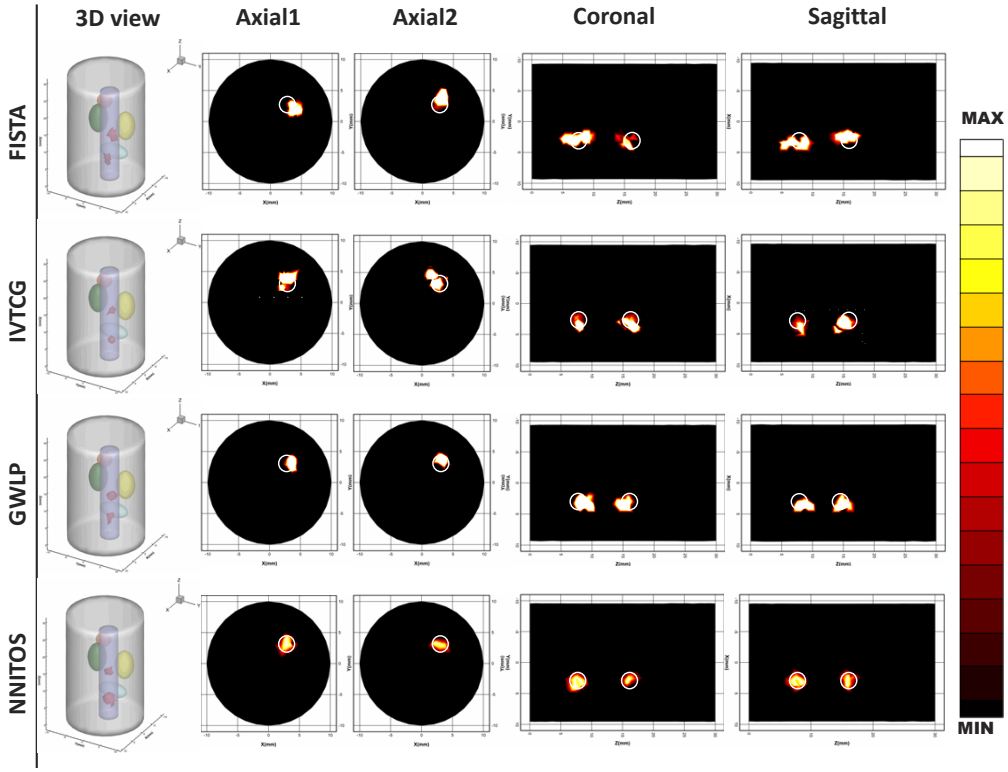

Fig. 6. The reconstruction results of dual-source simulation experiment. Four different methods to reconstruct the radiation source were displayed in 3D view, axial view, coronal view and sagittal view. In 3D view, the red region was the double source of reconstruction, and in the slice view, the location and size of the real source were depicted by white circles.

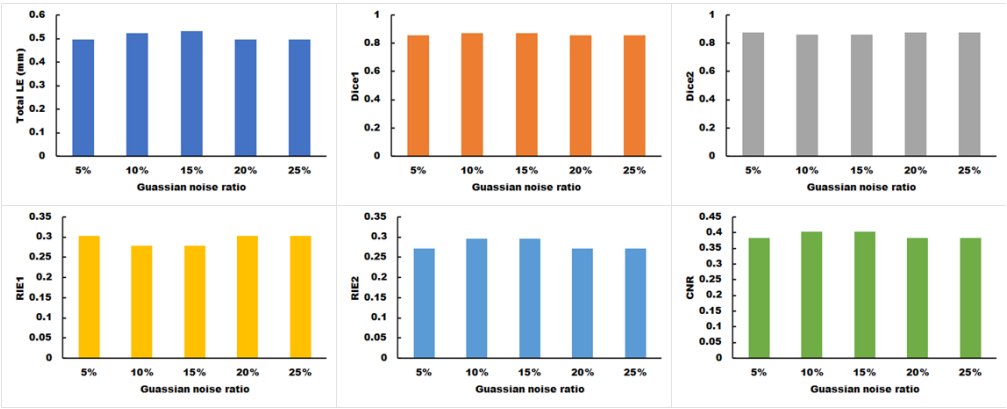

Fig. 7. The results of quantitative analysis of anti-noise experiment.

Optics EXPRESS

the reconstruction performance is better than other methods. The quantitative analysis of the reconstruction results of the real implanted animal experiment is shown in Table 6.

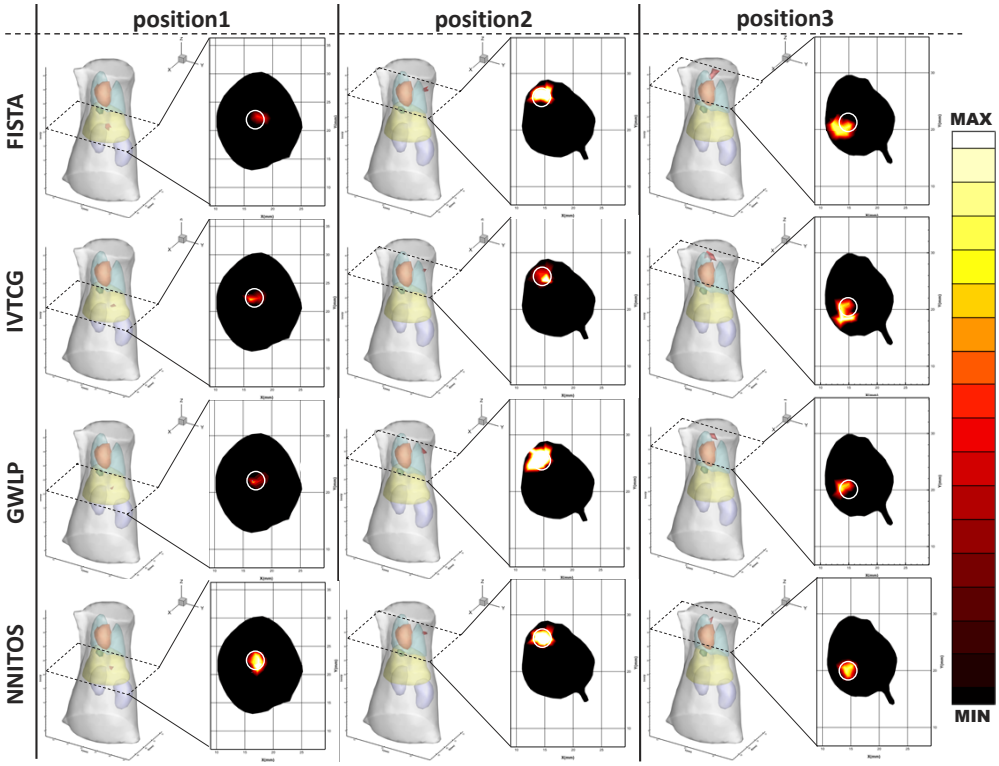

Fig. 8. Reconstruction results of different methods *in vivo* experiments. The box under the 3D viewing angle represents the cutting surface, and after the cutting plane was enlarged, the axial viewing plane on the right was obtained, and the white circle in the plane view was the real position and size of the Cerenkov source.

Table 6. Quantitative analysis of *in vivo* reconstruction results

No.	Actual source center (mm)	Method	LE (mm)	DICE	RIE	CNR
1	(17.5, 23.0, 21.0)	FISTA	0.853	0.324	1.491	0.077
		IVTCG	0.831	0.321	1.588	0.081
		GWLP	0.809	0.407	1.079	0.093
		NNITOS	0.221	0.681	0.314	0.102
2	(14.5, 26.0, 33.0)	FISTA	0.737	0.48	1.128	0.081
		IVTCG	0.625	0.764	1.205	0.084
		GWLP	0.524	0.753	0.897	0.085
		NNITOS	0.233	0.83	0.193	0.093
3	(14.5, 20.0, 36.0)	FISTA	0.879	0.5	0.893	0.078
		IVTCG	0.785	0.511	0.765	0.082
		GWLP	0.732	0.449	0.532	0.085
		NNITOS	0.2	0.632	0.108	0.092

Optics EXPRESS

4. Discussion and conclusion

CLT can be used to visualize the three-dimensional distribution of radioactive probes in living animals, which solves the problem of insufficient depth information in traditional CLI methods. At present, it is considered that CLT is a highly promising imaging technology for clinical application. However, due to the ill-posedness of the inverse problem caused by the strong scattering of Cerenkov light *in vivo*, the performance of CLT reconstruction is not satisfactory. Further improving the reconstruction performance is of great significance to promote the application of CLT in preclinical and clinical research. Therefore, this paper proposes an NNITOS method to achieve better CLT reconstruction performance. EN regularization combines the $L_{1/2}$-norm and manifold learning regularization to balance the sparsity, smoothness, and edge preservation of Cerenkov sources. Because the regularization term is complex, we use the NNITOS method to split the inverse problem into three operators: the least square operator, the $L_{1/2}$-norm operator, and the manifold learning operator to reduce the computational complexity. On this basis, we use the method of shrinking ROI, which shrinks ROI based on the prior information generated by the previous iteration, and further controls the sparsity of the reconstructed Cerenkov source. The non-negative constraint of each iteration also ensures the sparsity of the reconstructed Cerenkov source, reduces the error, and helps to improve the performance of CLT reconstruction.

To evaluate the performance of NNITOS in CLT reconstruction, we used FISTA, IVTCG and, GWLP methods to compare with NNITOS, and carried out numerical simulation and *in vivo* experiments. The experimental results show that: 1) multi-sized source and multi-shape source simulation experiments show that NNITOS also has advantages in restoring source shape. 2) Dual-source simulation experiments show that NNITOS guarantees high reconstruction localization accuracy. 3) NNITOS exhibits good robustness in experimental tests against noise. 4) All simulation experiments show that NNITOS has better intensity recovery ability for Cerenkov sources than other methods. 5) *In vivo* experiments demonstrate the feasibility of NNITOS in biomedical research.

In addition, we also find that the decrease of position error may not cause the increase of the DICE coefficient or the decrease of the RIE coefficient. That is, there is a situation in which the centers of two regions are very close, but there may be great differences in shape, size, or strength between them. For example, in the spherical single source reconstruction in multi-shape simulation, compared with the FISTA method, the IVTCG method has a lower location error, but a higher RIE coefficient. Compared with the GWLP, the IVTCG method has a higher location error, but a higher DICE coefficient. Compared with other methods, NNITOS performs very well in these three evaluation indicators.

Although the NNITOS strategy performs well in CLT reconstruction, it still has some shortcomings. Firstly, in the manifold learning regularization, to group these nodes, we must find out the k-nearest nodes of each node, which is the initial group, and then automatically adjust the grouping according to the threshold. The selection of k will affect the accuracy of manifold learning gradient calculation, k is larger, the calculation accuracy is greater, but it takes more time. Therefore, how to determine the value of k of the initial group in manifold learning needs further research. In addition, the regularization parameters of NNITOS and some other internal parameters are chosen empirically. It is necessary to propose an adaptive parameter selection algorithm to objectively set these parameters. Finally, the clinical application of CLT based on the NNITOS strategy needs to be further studied.

Overall, an EN regularization-based NNITOS strategy is proposed for CLT morphological reconstruction. Compared with other traditional methods mentioned above, the NNITOS strategy achieved more precise results in the localization and morphological recovery of radioactive probes. And it has good robustness in the reconstruction. We believe that this strategy is beneficial to the preclinical and clinical research of CLT and promotes the development of theoretical research of optical tomography.

Optics EXPRESS

Funding. National Key Research and Development Program of China (2019YFC1521102); National Natural Science Foundation of China (61701403, 61806164, 62101439, 61906154); China Postdoctoral Science Foundation (2018M643719); Natural Science Foundation of Shaanxi Province (2020JQ-601); Young Talent Support Program of the Shaanxi Association for Science and Technology (20190107); Key Research and Development Program of Shaanxi Province (2019GY-215, 2021ZDLSF06-04); Major research and development project of Qinghai (2020-SF-143); Young Innovation Team of Shaanxi Provincial Department of Education (21JP123).

Disclosures. The authors declare no conflicts of interest.

Data availability. Data underlying the results presented in this paper are not publicly available at this time but may be obtained from the authors upon request.

References

1. P. A. Cherenkov, "Visible luminescence of pure liquids under the influence of γ-radiation," (1934).
2. J. S. Cho, R. Taschereau, S. Olma, K. Liu, Y. C. Chen, C. K. Shen, R. M. van Dam, and A. F. Chatziioannou, "Cerenkov radiation imaging as a method for quantitative measurements of beta particles in a microfluidic chip," Phys. Med. Biol. **54**(22), 6757–6771 (2009).
3. W. Yang, W. Qin, Z. Hu, Y. Suo, R. Zhao, X. Ma, W. Ma, T. Wang, J. Liang, and J. Tian, "Comparison of Cerenkov luminescence imaging (CLI) and gamma camera imaging for visualization of let-7 expression in lung adenocarcinoma A549 Cells," Nucl. Med. Biol. **39**(7), 948–953 (2012).
4. C. Qin, J. Zhong, Z. Hu, X. Yang, and J. Tian, "Recent advances in Cerenkov luminescence and tomography imaging," IEEE J. Sel. Top. Quantum Electron. **18**(3), 1084–1093 (2012).
5. Z. Hu, X. Chen, J. Liang, X. Qu, D. Chen, W. Yang, J. Wang, F. Cao, and J. Tian, "Single photon emission computed tomography-guided Cerenkov luminescence tomography," J. Appl. Phys. **112**(2), 024703 (2012).
6. G. S. Mitchell, R. K. Gill, D. L. Boucher, C. Li, and S. R. Cherry, "In vivo Cerenkov luminescence imaging: a new tool for molecular imaging," Philos. Trans. R. Soc., A **369**, 4605–4619 (2011).
7. A. Ruggiero, J. P. Holland, J. S. Lewis, and J. Grimm, "Cerenkov luminescence imaging of medical isotopes," J. Nucl. Med. **51**(7), 1123–1130 (2010).
8. S. Y. Jeong, M. H. Hwang, J. E. Kim, S. Kang, J. C. Park, J. Yoo, J. H. Ha, S. W. Lee, B. C. Ahn, and J. Lee, "Combined Cerenkov luminescence and nuclear imaging of radioiodine in the thyroid gland and thyroid cancer cells expressing sodium iodide symporter: Initial feasibility study," Endocr J **58**(7), 575–583 (2011).
9. Y. Xu, E. Chang, H. Liu, H. Jiang, S. S. Gambhir, and Z. Cheng, "Proof-of-Concept Study of Monitoring Cancer Drug Therapy with Cerenkov Luminescence Imaging," Journal of Nuclear Medicine Official Publication Society of Nuclear Medicine **53**(2), 312–317 (2012).
10. M. R. Grootendorst, M. Cariati, S. Pinder, A. Kothari, M. Douek, T. Kovacs, H. Hamed, A. Pawa, F. Nimmo, and J. Owen, "Intraoperative Assessment of Tumor Resection Margins in Breast-Conserving Surgery using 18F-FDG Cerenkov Luminescence Imaging - A First-in-Human Feasibility Study," J. Nucl. Med. **116**, 181032 (2016).
11. H. Liu, X. Yang, T. Song, C. Bao, L. Shi, Z. Hu, K. Wang, and J. Tian, "Multispectral hybrid Cerenkov luminescence tomography based on the finite element SPn method," J. Biomed. Opt. **20**(8), 086007 (2015).
12. Changqing Li, Gregory S. Mitchell, and S. R. Cherry, "Cerenkov luminescence tomography for small-animal imaging," Opt. Lett. **35**(7), 1109 (2010).
13. X. Ding, K. Wang, B. Jie, Y. Luo, Z. Hu, and J. Tian, "Probability method for Cerenkov luminescence tomography based on conformance error minimization," Biomed. Opt. Express **5**(7), 2091 (2014).
14. H. Zhenhua, M. Liu, Z. Zhang, H. Guo, and J. Tian, "A novel radiopharmaceutical-excited fluorescence tomography of the mice bearing hepatocellular carcinoma," J. Nuclear Medicine **57**, 1421 (2016).
15. Zhong Jianghong, Tian Jie, YangChenghu Xin, and Qin, "Whole-Body Cerenkov Luminescence Tomography with the Finite Element SP3 Method," Ann. Biomed. Eng. **39**(6), 1728–1735 (2011).
16. Y. Xu, H. Liu, and Z. Cheng, "Harnessing the power of radionuclides for optical imaging: Cerenkov luminescence imaging," J. Nucl. Med. **52**(12), 2009–2018 (2011).
17. Z. Hu, J. Liang, W. Yang, W. Fan, C. Li, X. Ma, X. Chen, X. Ma, X. Li, and X. Qu, "Experimental Cerenkov luminescence tomography of the mouse model with SPECT imaging validation," Opt. Express **18**(24), 2441 (2010).
18. M. Cai, Z. Zhang, X. Shi, J. Yang, Z. Hu, and J. Tian, "Non-Negative Iterative Convex Refinement Approach for Accurate and Robust Reconstruction in Cerenkov Luminescence Tomography," IEEE Trans. Med. Imaging **39**(10), 3207–3217 (2020).
19. H. Guo, X. He, M. Liu, Z. Zhang, Z. Hu, and J. Tian, "Weight Multispectral Reconstruction Strategy for Enhanced Reconstruction Accuracy and Stability With Cerenkov Luminescence Tomography," IEEE Trans. Med. Imaging **36**(6), 1337–1346 (2017).
20. H. Guo, Z. Hu, X. He, X. Zhang, M. Liu, Z. Zhang, X. Shi, S. Zheng, and T. Jie, "Non-convex sparse regularization approach framework for high multiple-source resolution in Cerenkov luminescence tomography," Opt. Express **25**, 28068 (2017).
21. Bangerth and Wolfgang, "A Framework for the Adaptive Finite Element Solution of Large-Scale Inverse Problems," SIAM J. Sci. Comput. **30**(6), 2965–2989 (2008).

Optics EXPRESS

22. H. Meng, K. Wang, Y. Gao, Y. Jin, X. Ma, and J. Tian, "Adaptive Gaussian Weighted Laplace Prior Regularization Enables Accurate Morphological Reconstruction in Fluorescence Molecular Tomography," IEEE Trans. Med. Imaging **38**(12), 2726–2734 (2019).
23. H. Zhang, G. Geng, X. Wang, X. Qu, Y. Hou, and X. He, "Fast and robust reconstruction for fluorescence molecular tomography via regularization," BioMed Res. Int. **2016**, 5065217 (2016).
24. H. Guo, L. Gao, J. Yu, X. He, H. Wang, J. Zheng, and X. Yang, "Sparse-graph manifold learning method for bioluminescence tomography," J Biophotonics **13**(4), e201960218 (2020).
25. J. Zhao, H. Guo, J. Yu, H. Yi, Y. Hou, and X. He, "A robust elastic net-l1l2reconstruction method for x-ray luminescence computed tomography," Phys. Med. Biol. **66**(19), 195005 (2021).
26. H. Guo, J. Yu, X. He, H. Yi, Y. Hou, and X. He, "Total Variation Constrained Graph Manifold Learning Strategy for Cerenkov Luminescence Tomography," Opt. Express **30**(2), 1422–1441 (2022).
27. M. Cai, Z. Zhang, X. Shi, Z. Hu, and J. Tian, "NIR-II/NIR-I Fluorescence Molecular Tomography of Heterogeneous Mice Based on Gaussian Weighted Neighborhood Fused Lasso Method," IEEE Trans. Med. Imaging **39**(6), 2213–2222 (2020).
28. H. Zhang, X. Huang, M. Zhou, G. Geng, and X. He, "Adaptive shrinking reconstruction framework for cone-beam X-ray luminescence computed tomography," Biomed. Opt. Express **11**(7), 3717–3732 (2020).
29. P. Gao, K. Cheng, E. Schuler, M. Jia, W. Zhao, and L. Xing, "Restarted primal-dual Newton conjugate gradient method for enhanced spatial resolution of reconstructed cone-beam x-ray luminescence computed tomography images," Phys. Med. Biol. **65**(13), 135008 (2020).
30. W. Zhang, Z. Li, Z. Sun, K. Jia, and J. Feng, "Cherenkov-excited luminescence scanned tomography reconstruction based on Unet," in *Molecular-Guided Surgery: Molecules, Devices, and Applications VIII* (SPIE, 2022), pp. 101–108.
31. X. Wei, D. Lu, X. Cao, L. Su, L. Wang, H. Guo, Y. Hou, and X. He, "A fuzzy artificial neural network-based method for Cerenkov luminescence tomography," AIP Adv. **9**(6), 065105 (2019).
32. X. Zhang, C. Li, Z. Zhang, Z. Hu, and J. Tian, "Residual learning network for accurate and stable reconstruction in Cerenkov luminescence tomography," in *Medical Imaging 2022: Biomedical Applications in Molecular, Structural, and Functional Imaging* (SPIE, 2022), pp. 344–349.
33. Z. Zhang, M. Cai, Y. Gao, X. Shi, X. Zhang, Z. Hu, and J. Tian, "A novel Cerenkov luminescence tomography approach using multilayer fully connected neural network," Phys. Med. Biol. **64**(24), 245010 (2019).
34. X. Zhang, M. Cai, L. Guo, Z. Zhang, B. Shen, X. Zhang, Z. Hu, and J. Tian, "Attention mechanism-based locally connected network for accurate and stable reconstruction in Cerenkov luminescence tomography," Biomed. Opt. Express **12**(12), 7703–7716 (2021).
35. X. Cao, X. Wei, F. Yan, L. Wang, and X. He, "A Novel Stacked Denoising Autoencoder-Based Reconstruction Framework for Cerenkov Luminescence Tomography," IEEE Access **7**, 85178–85189 (2019).
36. A. Beck and M. Teboulle, "A fast iterative shrinkage-thresholding algorithm for linear inverse problems," SIAM J. Imaging Sci. **2**(1), 183–202 (2009).
37. X. He, J. Liang, X. Wang, J. Yu, X. Qu, X. Wang, Y. Hou, D. Chen, F. Liu, and J. Tian, "Sparse reconstruction for quantitative bioluminescence tomography based on the incomplete variables truncated conjugate gradient method," Opt. Express **18**(24), 24825–24841 (2010).
38. Y. Gao, K. Wang, S. Jiang, Y. Liu, T. Ai, and J. Tian, "Bioluminescence tomography based on Gaussian weighted Laplace prior regularization for in vivo morphological imaging of glioma," IEEE Trans. Med. Imaging **36**(11), 2343–2354 (2017).
39. A. D. Klose, "The forward and inverse problem in tissue optics based on the radiative transfer equation: A brief review," J. Quant. Spectrosc. Radiat. Transfer **111**(11), 1852–1853 (2010).
40. Y. Lv, J. Tian, W. Cong, G. Wang, J. Luo, W. Yang, and H. Li, "A multilevel adaptive finite element algorithm for bioluminescence tomography," Opt. Express **14**(18), 8211–8223 (2006).
41. W. Bangerth and A. Joshi, "Adaptive finite element methods for the solution of inverse problems in optical tomography," Inverse Problems **24**(3), 034011 (2008).
42. S. R. Arridge and J. C. Schotland, "Optical tomography: forward and inverse problems," Inverse problems **25**(12), 123010 (2009).
43. F. Bian and X. Zhang, "A three-operator splitting algorithm for nonconvex sparsity regularization," SIAM J. Sci. Comput. **43**(4), A2809–A2839 (2021).
44. G. Li and T. K. Pong, "Douglas–Rachford splitting for nonconvex optimization with application to nonconvex feasibility problems," Math. Program. **159**(1-2), 371–401 (2016).
45. H. Zou and T. Hastie, "Regularization and variable selection via the elastic net," J Royal Statistical Soc. B. **67**(2), 301–320 (2005).
46. P. Causin, G. Naldi, and R.-M. Weishaeupl, "Elastic net regularization in diffuse optical tomography applications," in *16th International Symposium on Biomedical Imaging (ISBI 2019)* (IEEE, 2019), pp. 1627–1630.
47. X. Liu, X. Kong, L. Qiao, and J. Zhao, "Efficient L1/2 regularization-based reconstruction for photoacoustic imaging using adaptively iterative thresholding algorithm," Journal of Medical Imaging and Health Informatics **10**(7), 1506–1514 (2020).
48. L. Chen, I. W. Tsang, and D. Xu, "Laplacian embedded regression for scalable manifold regularization," IEEE Trans. Neural Netw. Learning Syst. **23**(6), 902–915 (2012).

Optics EXPRESS

49. X. He, X. Wang, H. Yi, Y. Chen, X. Zhang, J. Yu, and X. He, "Laplacian manifold regularization method for fluorescence molecular tomography," J. Biomed. Opt. **22**(4), 045009 (2017).
50. J. Liu, D. He, X. Zeng, M. Wang, X. Xiu, W. Liu, and W. Li, "ManiDec: Manifold constrained low-rank and sparse decomposition," IEEE Access **7**, 112939–112952 (2019).
51. L. Yin, K. Wang, T. Tong, Q. Wang, Y. An, X. Yang, and J. Tian, "Adaptive Grouping Block Sparse Bayesian Learning Method for Accurate and Robust Reconstruction in Bioluminescence Tomography," IEEE Trans. Biomed. Eng. **68**(11), 3388–3398 (2021).
52. P. Yin, Y. Lou, Q. He, and J. Xin, "Minimization of 1-2 for compressed sensing," SIAM J. Sci. Comput. **37**(1), A536–A563 (2015).
53. S. Boyd, N. Parikh, E. Chu, B. Peleato, and J. Eckstein, "Distributed optimization and statistical learning via the alternating direction method of multipliers," FNT in Machine Learning **3**(1), 1–122 (2010).
54. D. Van Hieu, L. Van Vy, and P. K. Quy, "Three-operator splitting algorithm for a class of variational inclusion problems," Bull. Iran. Math. Soc. **46**(4), 1055–1071 (2020).
55. X. Cao, J. Zhang, J. Yang, C. Fan, F. Zhao, W. Zhou, L. Wang, G. Geng, M. Zhou, and X. Chen, "A deep unsupervised clustering-based post-processing framework for high-fidelity Cerenkov luminescence tomography," J. Appl. Phys. **128**(19), 193104 (2020).
56. B. Parvitte, C. Risser, R. Vallon, and V. Zéninari, "Quantitative simulation of photoacoustic signals using finite element modelling software," Appl. Phys. B **111**(3), 383–389 (2013).
57. Y. Yang, K. K. H. Wang, S. Eslami, I. I. Iordachita, M. S. Patterson, and J. W. Wong, "Systematic calibration of an integrated x-ray and optical tomography system for preclinical radiation research," Med. Phys. **42**(4), 1710–1720 (2015).
58. H. Yi, D. Chen, W. Li, S. Zhu, X. Wang, J. Liang, and J. Tian, "Reconstruction algorithms based on l1-norm and l2-norm for two imaging models of fluorescence molecular tomography: a comparative study," J. Biomed. Opt. **18**(5), 056013 (2013).